Research paper

Dynamic analysis and chaos control in heat-affected non-smooth brushless DC motors with load torque through genetic algorithms

Steve Tchassem Nkengne [a], Buris Peggy Ndemanou [b], André Chéagé Chamgoué [c], Dianorré Tokoue Ngatcha [d,*], Hilaire Bertrand Fotsin [a], Sifeu Takougang Kingni [b]

[a] Research Unit of Condensed Matter, Electronics and Signal Processing (UR-MACETS), Department of Physics, Faculty of Science, University of Dschang, P.O. Box 67, Dschang, Cameroon
[b] Department of Mechanical, Petroleum and Gas Engineering, National Advanced School of Mines and Petroleum Industries, University of Maroua, P.O. Box 46, Maroua, Cameroon
[c] Department of Petroleum and Gas Engineering, School of Geology and Mining Engineering, University of Ngaoundere, P.O. BOX 115, Meiganga, Cameroon
[d] Laboratory of Mechatronics, Energiatronics and Sustainable Mobility (LaMEMD), Department of Automotive and Mechatronics Engineering, National Higher Polytechnic School of Douala, University of Douala, P.O. Box 24, 2701, Douala, Cameroon

ARTICLE INFO

ABSTRACT

The objective of this paper is to study the dynamics, microcontroller validation, and annihilation of chaos by using the genetic algorithms (GAs) to optimize parameters in the heat-affected non-smooth air-gap Brushless direct current motor (HNBDCM) with load torque. Stability analysis of steady-state of HNBDCM with load torque (HNBDCMLT) results in three steady states with stable and unstable branches in three considered planes. Hopf bifurcation, coexisting attractors, antimonotonicity, chaotic bubble characteristics, five different shapes of chaotic characteristics, and periodic characteristics are encountered in HNBDCMLT. These dynamical characteristics encountered during the numerical simulations are attested by the microcontroller execution of HNBDCMLT. Chaos annihilation in HNBDCMLT through parameter optimization thanks to the GAs is demonstrated because by optimizing some parameters of HNBDCMLT via GAs, the chaotic characteristics encountered in HNBDCMLT converged to one of its three steady states.

1. Introduction

Brushless direct current motors (BDCMs) play a crucial role in many industrial and domestic applications [1]. They feature simplicity of control, a wide speed range, and the ability to provide high torque at low speeds [2,3]. Historically, BDCMs have been widely studied, particularly for their use in applications such as electric traction, maritime propulsion systems, and laboratory equipment [1,4]. However, despite their robustness and versatility, the performance of BDCMs is strongly influenced by temperature and load torque during operation and/or manufacturing [2–4]. A nonsmooth-air-gap brushless direct current (NBLDC) motor is significantly affected by temperature and can be effectively analyzed using a microcontroller [5]. Heat produced within the motor is transmitted through the air gap to the magnets and housing, dissipating into the surroundings through the conductive copper windings that are part of the motor's structure [6]. The motor's performance can vary considerably between "cold" and "hot" states, emphasizing the critical role of temperature [7]. Cooling techniques, such as using coolant flow or incorporating finned housings, can lower the motor's temperature by as much as 15% [8]. The design of the air gap between the rotor magnets and the stator core is

* Corresponding author.
  E-mail address: tokouengatcha1@gmail.com (D.T. Ngatcha).

essential for optimizing efficiency and magnetic strength. Furthermore, imbalances in phase-to-phase voltage within the three-phase power supply can result in increased heat production. NBLDC motors are utilized in a wide range of industries, including aerospace, automotive, household appliances, medical equipment, industrial automation, and instrumentation. The influence of temperature on BDCMs has been a subject of study for several decades [3,9]. It is well established that increasing temperature results in a decrease in winding resistance. This can result in variations in engine performance characteristics, including speed, efficiency, and component life [10]. Additionally, excessive heat can accelerate the aging of insulating materials, increasing the risk of motor failure [11,12]. Recent studies have explored sophisticated thermal models to predict the effects of temperature on motor losses and efficiency, highlighting the importance of effective cooling and thermal management strategies [13,14].

Load torques can be classified into two categories: active and passive load torques [15]. Active load torques are those that can drive the motor under equilibrium conditions, retaining their sign even when the direction of rotation changes. In contrast, passive load torques always oppose the motion and reverse their sign when the motion is reversed, such as torque due to friction cutting. There are several components of load torques [16], including friction torque, which represents the equivalent value of various frictional forces acting on the motor shaft; windage torque, which is the opposing torque generated by wind resistance when the motor is running; and the torque required to perform useful mechanical work. The nature of the torque can vary depending on the type of load, being constant and independent of speed, a function of speed, or exhibiting time-invariant or time-variant characteristics, with its behavior potentially changing based on the load's operational mode. Temperature plays a crucial role in the performance of brushless direct current BDCMs, especially regarding torque. As the temperature increases, the motor's resistance also rises [17,18], resulting in reduced torque output due to greater power losses, often referred to as Joule heating. Furthermore, the flux density of the permanent magnets decreases with higher temperatures, which, when combined with the increased resistance, can lead to a further decline in locked-rotor torque. Additionally, this rise in resistance and drop in flux density may result in an increase in the no-load speed of the motor. Generally, the maximum ambient temperature for most DC motors is between 85 °C and 100 °C, while the maximum winding temperature ranges from 100 °C to 125 °C [19]. At the same time, the load torque applied to the motor directly influences the thermal operating conditions [20,21]. An increase in load torque leads to an increase in current flowing through the windings, which in turn increases ohmic losses and heat dissipation [22,23]. Researchers have demonstrated that motors subjected to high and variable loads experience thermal cycling which can induce mechanical stress and reduce motor reliability [24,25]. Analyzing the behavior of BDCMs under various load conditions is essential to understanding their long-term performance, particularly in environments where load cycles are frequent and unpredictable [26–28].

Analytical and numerical studies of BDCMs have been developed to estimate the individual impacts of temperature and load torque [25–27]. While there are few studies in the literature on BDCMs that integrate thermal and load torque effects in a coherent manner [29]. The combination of these two factors presents a complex challenge for the optimization of BDCMs. Thus, this paper aims to comprehensively explore the combined effects of temperature and load torque on the performance of NBDCM. Section 2 examines HNBDCMLT analytically and numerically as well as the microcontroller execution of NBDCM under the combined effects of temperature and load torque. Possible strategies to control and if possible optimize the performance of HNBDCMLT via genetic algorithms for parameter optimization are discussed in Section 3. Section 4 presents the conclusion.

2. Theoretical and microcontroller probing of HNBDCMLT

The dimensionless equations of the HNBDCMLT are described in [2,11,14]:

$$\frac{di_q}{dt} = -\gamma (1 + \alpha\theta) i_q - i_d\omega + \rho\omega, \tag{1a}$$

$$\frac{di_d}{dt} = -\delta\gamma (1 + \alpha\theta) i_d + i_q\omega, \tag{1b}$$

$$\frac{d\omega}{dt} = \sigma (i_q - \omega) + \eta i_d i_q - T_l, \tag{1c}$$

where t the time, $i_{d,q}$ the dimensionless currents along the direct-quadrature (d-q) axis of the motor, ω the angle speed, θ (in °C) the temperature of the stator winding resistance, δ the ratio of the stator inductors along the d-q axis L_d and L_q, η the difference of the stator inductors along the d-q axis L_d and L_q, T_l the dimensionless mechanical load torque and $\alpha, \gamma, \rho, \sigma$ the dimensionless parameters. System (1) is dissipative because $\nabla V = \partial\left(di_q/dt\right)/\left(\partial i_q\right) + \partial\left(di_d/dt\right)/\left(\partial i_d\right) + \partial\left(d\omega/dt\right)/\left(\partial\omega\right) = -\left[\sigma + \gamma (1 + \delta)(1 + \alpha\theta)\right]$. The steady states $S\left(i_q^*, i_d^*, \omega^*\right)$ are deduced when the derivatives of system (1) are set to zero:

$$i_q^* = \rho\delta\gamma (1 + \alpha\theta) \omega * / \left[(\omega *)^2 + \delta\gamma^2 (1 + \alpha\theta)^2\right], \tag{2a}$$

$$i_d^* = \rho (\omega *)^2 / \left[(\omega *)^2 + \delta\gamma^2 (1 + \alpha\theta)^2\right], \tag{2b}$$

$$\begin{aligned}&-\sigma (\omega *)^5 - T_l (\omega *)^4 + \delta\gamma (1 + \alpha\theta) \left[\rho (\eta\rho + \sigma) - 2\sigma\gamma (1 + \alpha\theta)\right] (\omega *)^3 \\ &-2\delta\gamma^2 T_l (1 + \alpha\theta)^2 (\omega *)^2 + \sigma\delta^2\gamma^3 (1 + \alpha\theta)^3 \left[\rho - \gamma (1 + \alpha\theta)\right] (\omega *) - \delta^2\gamma^4 T_l (1 + \alpha\theta)^4 = 0.\end{aligned} \tag{2c}$$

Based on the values of parameters $\sigma, \delta, \eta, \rho, \theta$, and α, the steady states $S_i\left(i_q^*, i_d^*, \omega^*\right)$ are obtained by solving Eq. (2c). The characteristic equation of $S_i\left(i_q^*, i_d^*, \omega^*\right)$ is:

$$\begin{aligned}&\lambda^3 + \left[\sigma + \gamma (1 + \delta)\right](1 + \alpha\theta) \lambda^2 - \left\{\rho\sigma + \eta\left(i_d^{*2} - i_q^{*2}\right) - \omega^{*2} - \sigma.i_d + \rho.\eta.i_d^* - \gamma\left[\sigma + \sigma\delta + \gamma\delta (1 + \alpha\theta)\right](1 + \alpha\theta)\right\} \lambda + \\ &\sigma\omega^{*2} + \sigma i_q\omega^* + 2\eta i_d^* i_q^*\omega^* - \eta\rho i_q^*\omega^* + \eta\gamma\delta i_d^{*2} + \gamma\left[\delta\gamma\sigma (1 + \alpha\theta) - \delta\eta\rho i_d^* + \delta\eta i_d^{*2} - \delta\rho\sigma + \delta\sigma i_d^* - \eta i_q^{*2}\right](1 + \alpha\theta) = 0.\end{aligned} \tag{3}$$
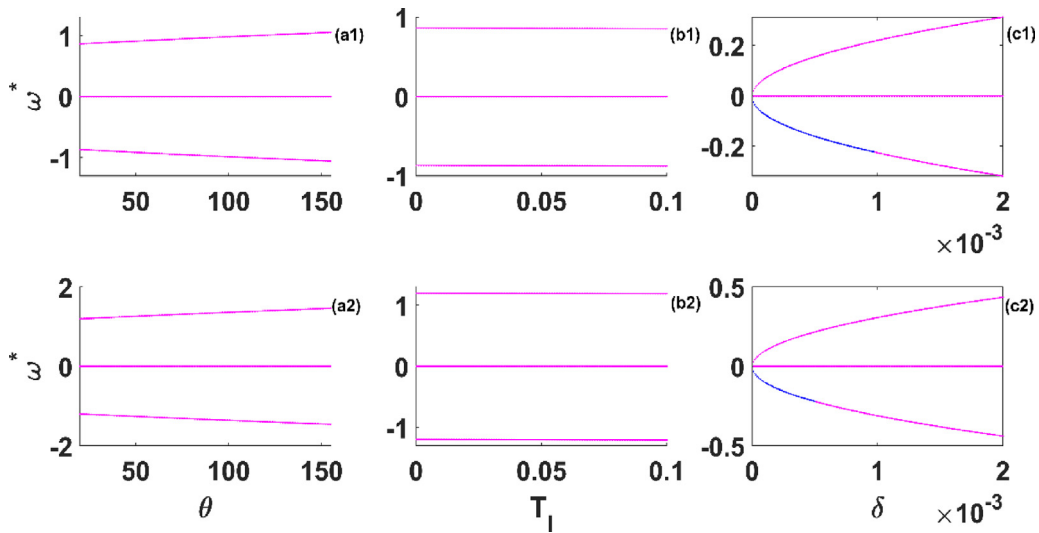
Fig. 1. Stability diagram of steady states in the planes: (a) (θ, ω^*) for $\delta = 0.015$, $T_l = 0.025$, (b) (T_l, ω^*) for $\delta = 0.015$, $\theta = 20$ and (c) (δ, ω^*) for $\theta = 20$, $T_l = 0.025$. In the first line $\eta = 0.1$ while in the second line $\eta = 0.26$ and the other parameters are $\gamma = 1/3$, $\sigma = 4.55$, $\rho = 60$ and $\alpha = 0.00393$. The cyan dots represent the unstable steady state while the blue dots represent the stable steady state.

The stability of System (1) depends on the solution of Eq. (3). Then to be stable, ensure that all the roots of Eq. (3) have a negative real part by using the Routh Hurwitz criteria. This gives:

$$[\sigma + \gamma(1+\delta)](1+\alpha\theta) > 0, \tag{4a}$$

$$\begin{aligned}
&\sigma\omega^{*2} + \sigma i_q\omega^* + 2\eta i_d^* i_q^* \omega^* - \eta\rho i_q^* \omega^* + \eta\gamma\delta i_d^{*2} + \\
&\gamma\left[\delta\gamma\sigma(1+\alpha\theta) - \delta\eta\rho i_d^* + \delta\eta i_d^{*2} - \delta\rho\sigma + \delta\sigma i_d^* - \eta i_q^{*2}\right](1+\alpha\theta) > 0
\end{aligned} \tag{4b}$$

$$\begin{aligned}
&[\sigma + \gamma(1+\delta)](1+\alpha\theta)\left\{\left\{-\rho\sigma - \eta\left(i_d^{*2} - i_q^{*2}\right) + \omega^{*2} + \sigma i_d - \rho\eta i_d^* + \gamma\left[\sigma + \sigma\delta + \gamma\delta(1+\alpha\theta)\right](1+\alpha\theta)\right\}\right\} - \\
&\left\{\sigma\omega^{*2} + \sigma i_q\omega^* + 2\eta i_d^* i_q^* \omega^* - \eta\rho i_q^* \omega^* + \eta\gamma\delta i_d^{*2} + \gamma\begin{bmatrix}\delta\gamma\sigma(1+\alpha\theta) - \delta\eta\rho i_d^* + \delta\eta i_d^{*2} - \delta\rho\sigma + \\ \delta\sigma i_d^* - \eta i_q^{*2}\end{bmatrix}(1+\alpha\theta)\right\} > 0
\end{aligned} \tag{4c}$$

The steady states stability in three considered planes is depicted in Fig. 1.

The three steady states $S_i\left(i_q^*, i_d^*, \omega^*\right)$ of Fig. 1 (a1), (a2), (b1) and (b2) are all unstable. In Fig. 1 (c1), there are three steady states where two steady states are unstable and the other steady state is stable in $0 \leq \delta \leq 0.00075$ whereas it is unstable in $0.00075 \leq \delta \leq 0.05$. So, this steady state has a transcritical or Hopf bifurcation at $\delta = 0.00075$. There are three steady states in Fig. 1 (c2) where two steady states are unstable and the other steady state is stable in the range $0 \leq \delta \leq 0.0005$ whereas it is unstable in the range $0.0005 \leq \delta \leq 0.05$. So, this steady state has a transcritical or Hopf bifurcation at $\delta = 0.0005$.

Given $X(t) = \left(x_1(t), \cdots, x_n(t)\right)$ with the n-dimensional vectorial flow $\left(F_1, \cdots, F_n\right)$, the overview of a set of first order differential system is written:

$$\frac{dX(t)}{dt} = F(t, x(t)), \text{ with } X(t_0) = X_0, \tag{5}$$

compared with the set of Eq. (1) results as: $x_1(t) = i_q$, $x_2(t) = i_d$, and $x_3(t) = w$ in 3-dimensions. The 4th-order Runge–Kutta (RK4) algorithm employed in integrating system (5) is as follows:

$$X_{i+1,j} = X_{i,j} + h\left(L_{1,j} + 2L_{2,j} + 2L_{3,j} + L_{4,j}\right)/6, \tag{6a}$$

$$t = t + h \tag{6b}$$

with;

$$L_{1,j} = F_j\left(t_i, X_{i,j}\right); \tag{7a}$$

$$L_{2,j} = F_j\left(t_i + \frac{h}{2}, X_{i,j} + \frac{h}{2}L_{1,j}\right); \tag{7b}$$

$$L_{3,j} = F_j\left(t_i + \frac{h}{2}, X_{i,j} + \frac{h}{2}L_{2,j}\right); \tag{7c}$$

$$L_{4,j} = F_j\left(t_i + h, X_{i,j} + hL_{3,j}\right); \tag{7d}$$
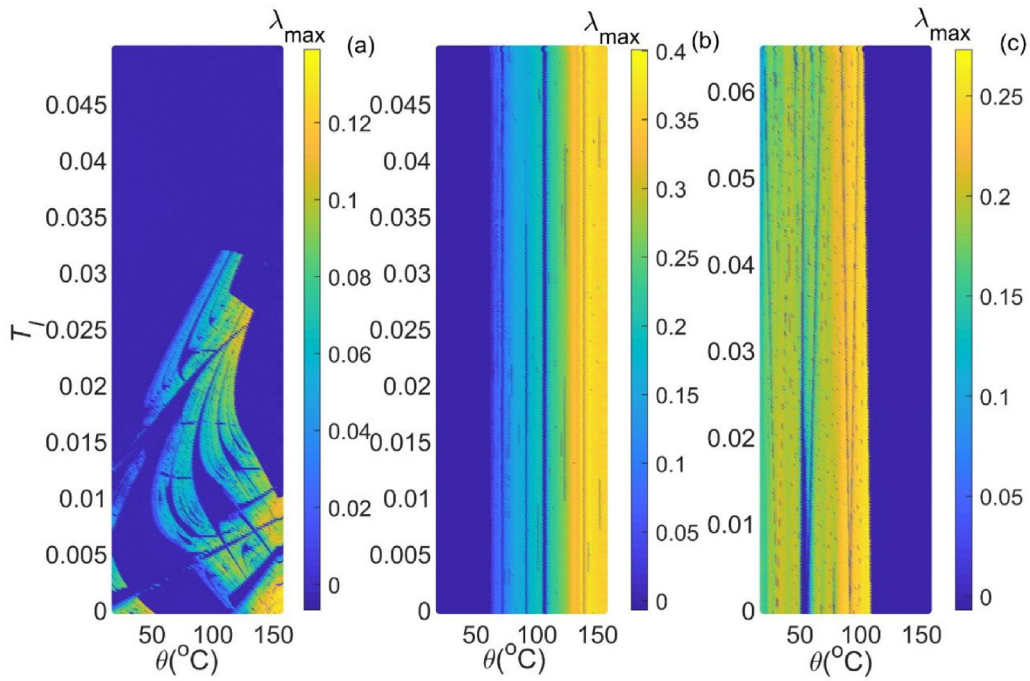
Fig. 2. Holistic dynamics of the model in the axis (θ, T_l) (a) $\delta = 0.015$, $\eta = 0.26$, (b) $\delta = 0.065$, $\eta = 0.26$, and (c) $\delta = 0.065$, $\eta = 0.1$ for $\rho = 60$, $\alpha = 0.00393$, $\sigma = 4.55$, and $\gamma = 1/3$. Initial associated states are: $(i_q(0), i_d(0), \omega(0)) = (0.01, 0.01, 0.01)$.

for i, which runs with time step and j labels the variables related to X_j, $L_{1,j}$, $L_{2,j}$, $L_{3,j}$, and $L_{4,j}$ which are intermediate coefficients of the RK4 algorithm and h the time step size which in the course of this paper was kept constant at 0.001. If we approximate two initially nearby state variables $X(t_0)$ and $X(t_0) + \delta X(t_0)$ to the system (5), the deviation $\delta X(t)$ evolves as:

$$\frac{d\delta X(t)}{dt} = \left[\frac{\delta F}{\delta X}\right]_{X_0} . \delta X, \text{ with } \delta X(t_0) = \delta X_0, \tag{8}$$

where $\left[\frac{\delta F}{\delta X}\right]$ is the Jacobian of the flow F evaluated on X_0. The nth eigenvalues of this Jacobian are referred to as Lyapunov exponents and they are numerically determined by employing the following equation:

$$\lambda_k = \lim_{t \to +\infty} \frac{1}{t} \ln\left[\frac{|\delta x_k(t)|}{\delta x_k(0)}\right], \text{ with } k = 1, \ldots, 3 \text{ in our case.} \tag{9}$$

And the sign of λ_k directly indicates chaoticity when positive and periodic behavior when negative.

The dynamical characteristics of System (1) in the plane (θ, T_l) are illustrated in Fig. 2.

The exposure in Fig. 2 defines the Largest Lyapunov exponents (LLE) $\lambda_{\max}$ of System (1). The positive LLE $(\lambda_{\max} > 0)$ validates the presence of chaotic structures in the System (1), while the negative LLE $(\lambda_{\max} < 0)$ validates the presence of periodic oscillations. As the plane (θ, T_l) is progressively screened, the model exhibits a combination of chaotic structures and periodic oscillations detailing the large-scale dynamics in the model. Chaotic structures dominate the model at extreme temperatures and low load torque, however, the keen observation remains that periodic oscillations predominate the model, as uncovered by the large portion of deep blue shades in Fig. 2 (a) for given parameter values. Furthermore, for $T_l > 0.035$, there are no reported chaotic structures in the model as unveiled in Fig. 2 (a). Chaotic structures dominate Fig. 2 (b) for increasing $\delta = 0.065$, with periodic oscillations at low temperatures. When the parameters $\delta = 0.065$ and $\eta = 0.1$ are varied as unveiled in Fig. 2 (c), the trend is contrary to the already observed trend in which complex structures are observed at low temperatures ≤ 100 °C. The bifurcation structures of i_q and LLE with respect of θ are depicted in Fig. 3.

Period-2-oscillations, period doubling to chaos, and interceptions of chaos by periodic characteristics are the dynamical exposure of the HNBDCMLT in Fig. 3 (a) endorsed by the LLE of Fig. 3 (b). The bifurcation structures and LLE plots respect to δ are depicted in Fig. 4.

Fig. 4 (a) displays no oscillations up to 0.00075 where a Hopf bifurcation appears at $\delta = 0.00075$, then limit cycle and period doubling to chaos region with interceptions of periodic characteristics. The dynamical characteristics encountered in Fig. 4 (a) are confirmed by the LLE of Fig. 4 (b). The bifurcation structures of i_q and LLE with respect to T_l are depicted in Fig. 5.

The coexistence between period-4-oscillations and chaotic characteristics, period-4-oscillations, reverse period doubling to chaos followed by coexistence between period-2-oscillations and limit cycle, limit cycle, period-2-oscillations, and limit cycle are the dynamical exposure of
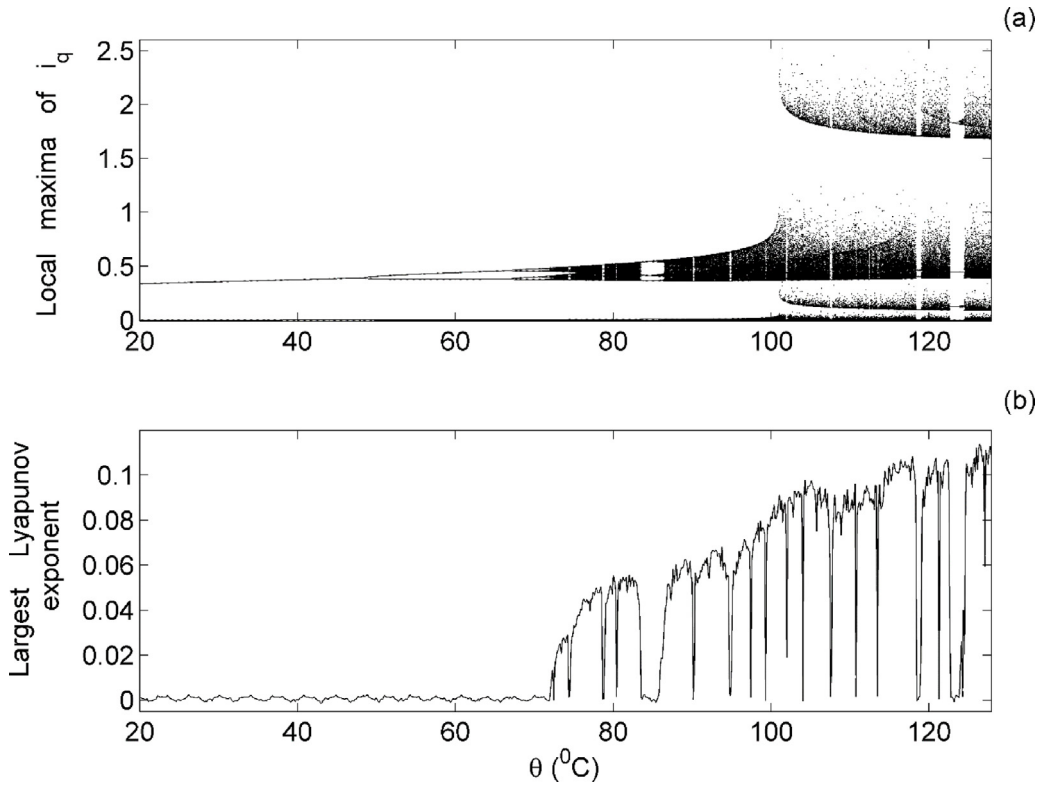
Fig. 3. Bifurcation diagram of i_q and LLE against the temperature θ for $T_l = 0.025$, $\gamma = 1/3$, $\sigma = 4.55$, $\eta = 0.26$, $\delta = 0.015$, $\rho = 60$, $\alpha = 0.00393$ and starting conditions $\left(i_q(0) = 0.01, i_d(0) = 0.01, \omega(0) = 0.01\right)$.
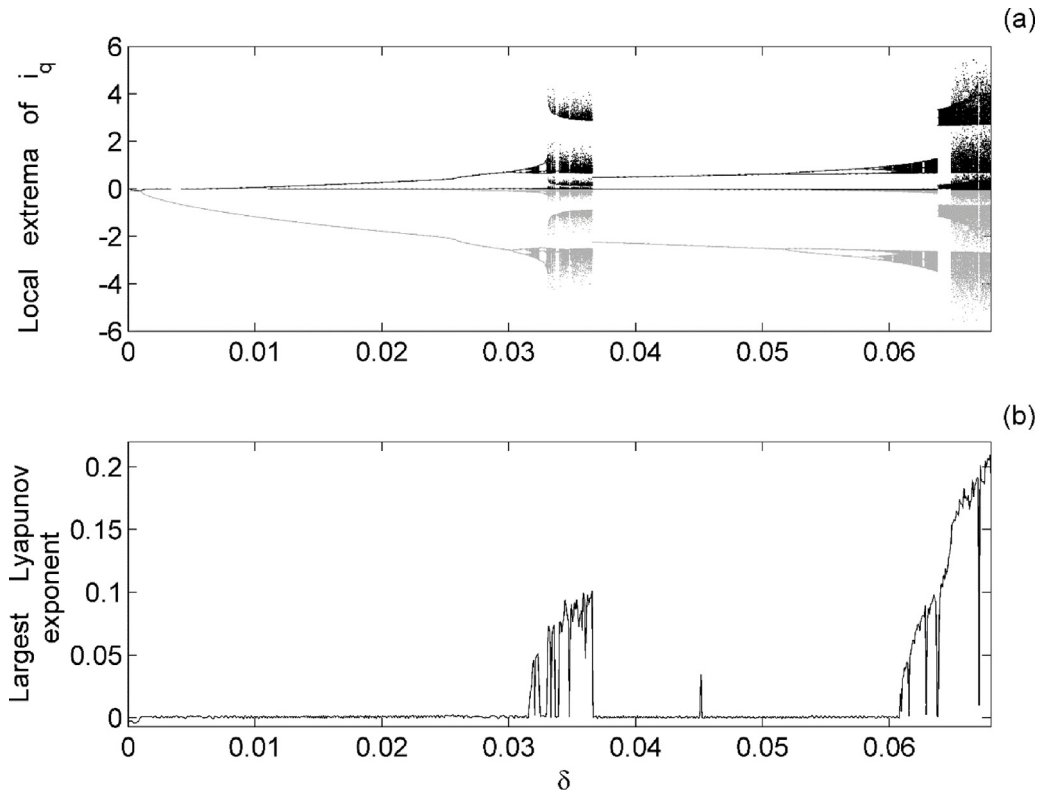

Fig. 4. Local extrema of i_q(a) and LLE (b) respect to δ for $\theta = 20$ °C, $\gamma = 1/3$, $\sigma = 4.55$, $\eta = 0.1$, $T_l = 0.025$, $\rho = 60$, $\alpha = 0.00393$ and starting conditions $\left(i_q(0) = 0.01, i_d(0) = 0.01, \omega(0) = 0.01\right)$. Local maxima and minima give the black and gray dots, respectively.
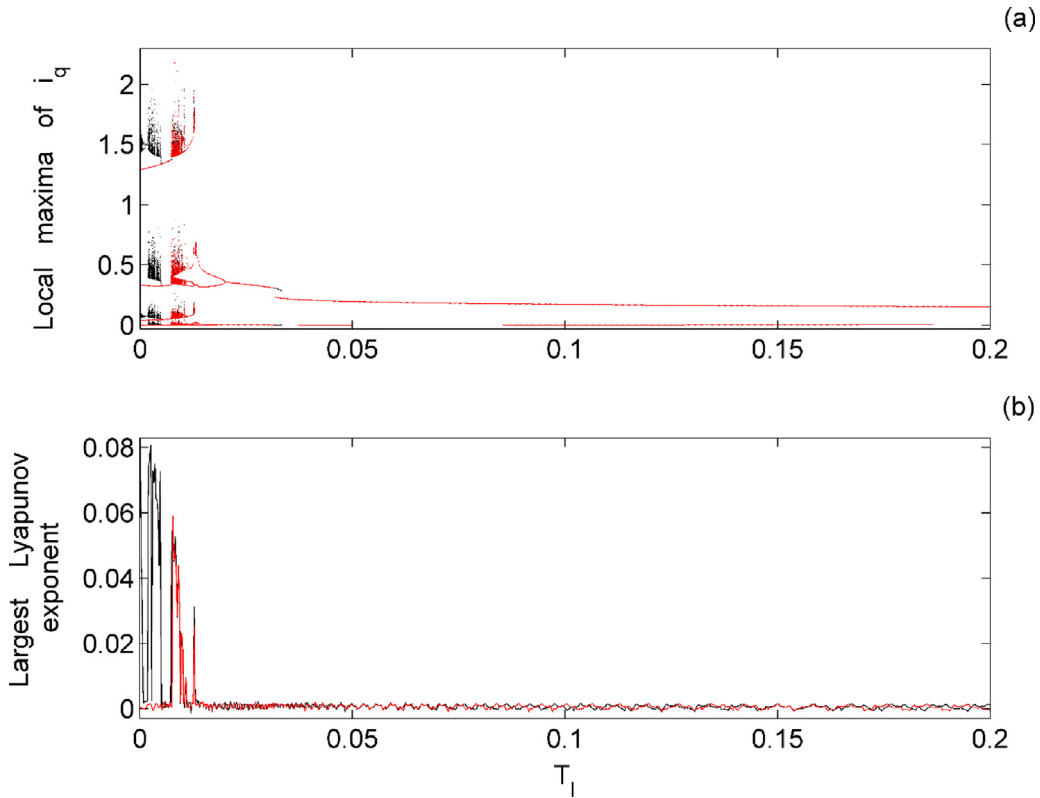
Fig. 5. Bifurcation diagrams of i_q and the corresponding LLE against the load torque T_l for $\theta = 20$ °C, $\gamma = 1/3$, $\sigma = 4.55$, $\eta = 0.26$, $\delta = 0.015$, $\rho = 60$, $\alpha = 0.00393$ and starting conditions $(i_q(0) = 0.01, i_d(0) = 0.01, \omega(0) = 0.01)$. Decreasing and increasing T_l respectively give rise to the red and black plots.

HNBDCMLT in Fig. 5 (a) endorsed by the LLE of Fig. 5 (b). The bifurcation structures of i_q with respect of T_l are depicted in Fig. 6 for specific values of parameter η.

The antimonotonicity phenomenon is shown in Fig. 5 which is characterized by bubbles of period-2-oscillations in Fig. 6 (a), bubbles of period-4-oscillations in Fig. 6 (b), bubbles of period-8-oscillations in Fig. 6 (c), bubbles of period-16-oscillations in Fig. 6 (d), chaotic bubbles in Fig. 6 (e) and (f) and finally chaotic oscillations in Fig. 6 (g) and (h). The phase portraits of Fig. 7 illustrate the dynamical characteristics reported in Figs. 3 to 6.

No oscillations are depicted in Fig. 7 (a), limit cycle is exhibited in Fig. 7 (b), and four different shapes of chaotic characteristics are illustrated in Fig. 7 (c to f), coexisting characteristics between period-4-oscillations and chaotic characteristics are presented in Fig. 7 (g1) and (g2), and chaotic bubble characteristic is shown in Fig. 7 (h). The coexisting characteristics unveil in system (1) are further proven in Fig. 8.

Regular characteristics are obtained with the commencing states specified by red regions while chaos is generated with the commencing states exposed in black regions as illustrated in Fig. 8.

The microcontroller execution of the HNBDCMLT is illustrated in Fig. 9.

To carry out the microcontroller implementation of the HNBDCMLT described by System (1), Fig. 9 is equipped with an Arduino card of the Mega 2560 type, resistors mounted in bridges of values R and 2R, and an analog oscilloscope whose inputs are equipped with capacitors to ensure the filtering of spurious signals. Microcontrollers are distinguished from other computing devices by their programmability. Often referred to as "special purpose computers", they are designed to execute specific tasks stored in their read-only memory (ROM). With integrated memory and input/output (I/O) ports, they simplify design by eliminating the need for external components like RAM and peripheral chips, which are typically required in simulation tools such as PSIM or OrCAD-PSpice. Additionally, microcontrollers are cost-effective and energy-efficient, making them suitable for a wide range of embedded applications. Their compact size and low power consumption allow for easy integration into devices, from household appliances to industrial machinery. As highlighted in the work of Ngongiah et al. [30], these features make microcontrollers a practical choice for advancing innovative technologies across various sectors and this method of implementation permits the comparison of results. The microcontroller results of HNBDCMLT obtained from Fig. 9 are established in Fig. 10.

The microcontroller results in Fig. 10 present a good qualitative correlation with the numerical results in Fig. 7 (b) to (h).
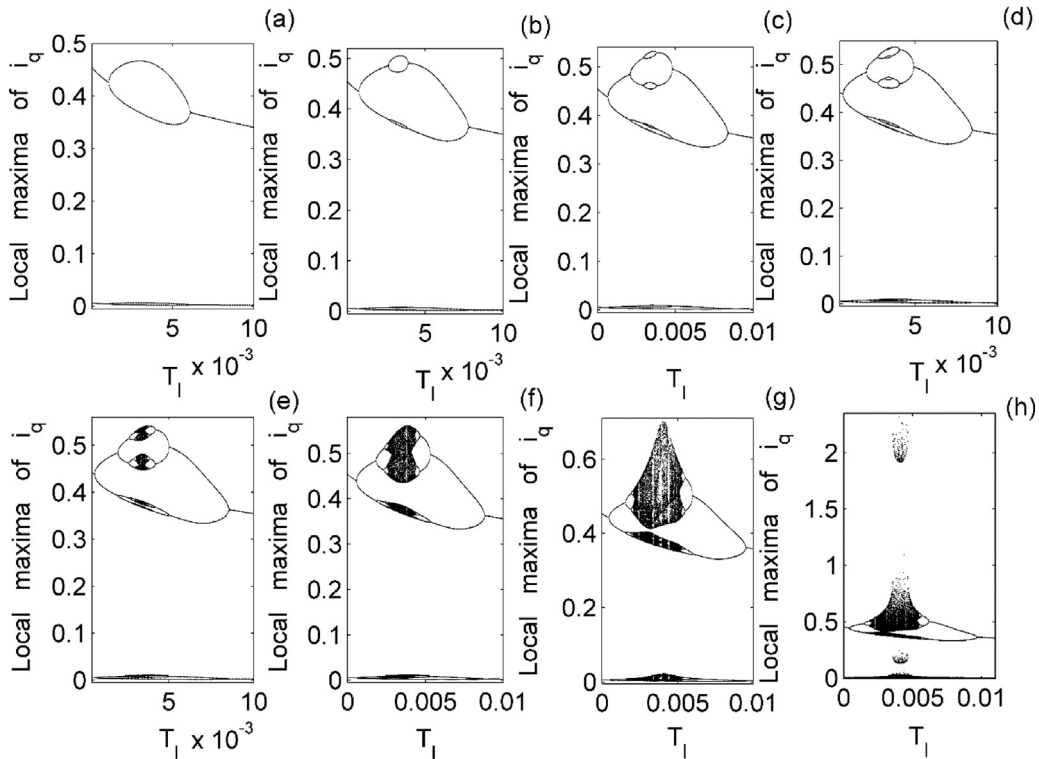
Fig. 6. Bifurcation diagrams of i_q and the corresponding LLE against the load torque T_l for given values of parameter η: (a)$\eta = 0.19$, (b)$\eta = 0.2$, (c)$\eta = 0.2036$, (d)$\eta = 0.204$, (e)$\eta = 0.2044$, (f)$\eta = 0.206$, (g)$\eta = 0.2099$, and (h)$\eta = 0.211$. $\theta = 20\ °C$, $\gamma = 1/3$, $\sigma = 4.55$, $\eta = 0.26$, $\delta = 0.015$, $\rho = 60$, $\alpha = 0.00393$ are the other parameters with starting conditions $\left(i_q(0) = 0.01, i_d(0) = 0.01, \omega(0) = 0.01\right)$.

3. Chaos annihilation in HNBDCMLT via parameter optimization using the GAs

Various facets of chaotic schemes have been documented in the literature, showcasing a range of control strategies that include, but are not limited to, backstepping control, adaptive control, contraction theory-based control, and sliding mode control (SMC). Among these methodologies, SMC stands out as particularly noteworthy due to its robust performance in managing uncertainties and nonlinearities within chaotic systems. These control strategies highlighted face the challenge of integration or differentiation as presented by Ngongiah et al. [30] and included citations. Artificial intelligence and optimization algorithms are being increasingly employed to assist in determining controller parameters for managing chaos in dynamic systems [31–33]. These promising methods offer interesting perspectives for the development of real-time control systems [34–36]. Controlling chaos by employing genetic algorithms (GAs) to optimize system parameters has the advantage of not requiring knowledge of the derivation or integration of the optimization system being investigated [37]. The chaotic characteristics observed in HNBDCMLT are suppressed through parameter optimization using genetic algorithms (GAs) in this section.

The setup for optimizing parameters using genetic algorithms typically involves several key components and steps:

In this paper, the HNBDCMLT system is clearly presented with analytical calculations for the steady states and its dynamical characteristics.

The GA scheme generates an initial sample of potential solutions, each representing a set of parameters for the HNBDCMLT system. This initial sample is randomly created within specified bounds.

The fitness function is then defined to evaluate how well each parameter set performs in controlling the HNBDCMLT system. This function often measures the objective, such as minimizing error or maximizing stability.

Genetic Algorithm Operations in stages including:

Selection involves evaluate the fitness of each parameter set in the HNBDCMLT system. Select the best-performing parameter set based on their fitness scores using methods like tournament selection or roulette wheel selection.

Crossover is depicted by pairing selected parameters to create new parameters by combining their parameter sets. This process mimics biological reproduction, allowing for the sharing of successful traits.

Mutation then introduces random variations to some new parameters to maintain diversity in the parameter sets and explore new areas of the solution space.

Iteration then further repeat the selection, crossover, and mutation processes for multiple generations. Regarding each iteration, the new parameter set are evaluated by employing the fitness function and the best solutions is retained. This iterative cycle continues
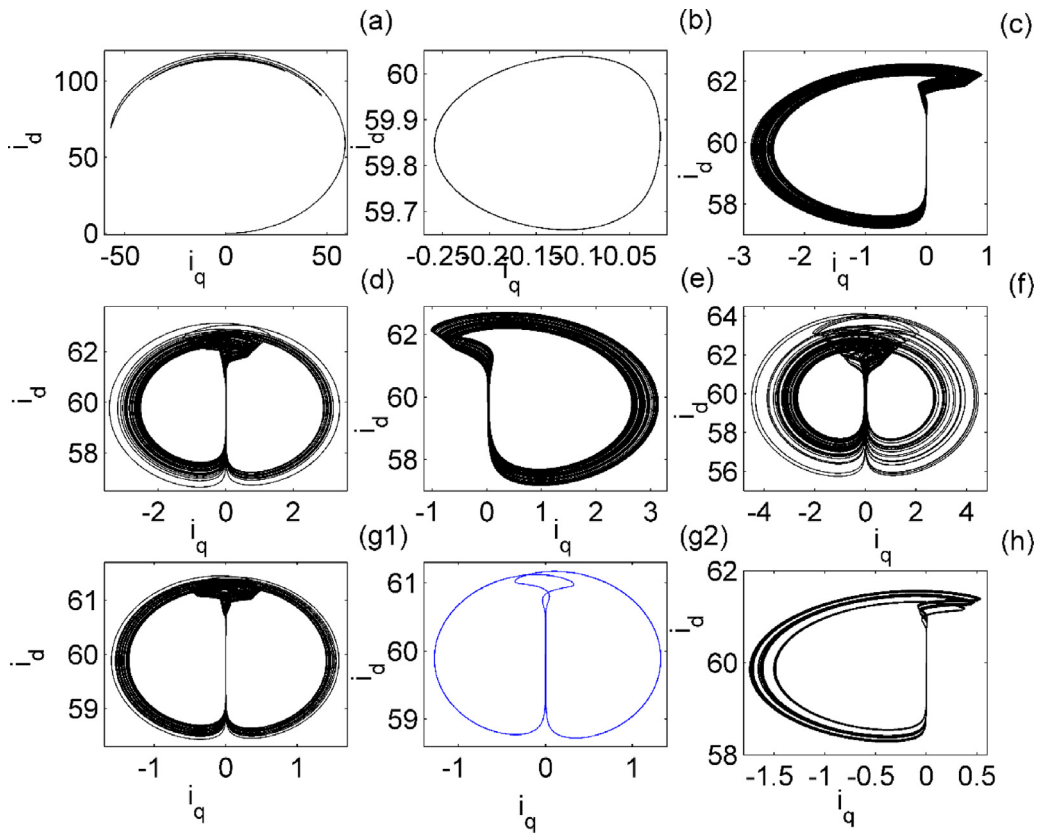
Fig. 7. Phase portraits of system Eq. (1) for (a) $\delta = 0.0006$, $\eta = 0.1$, $T_l = 0.025$, (b) $\delta = 0.0014$, $\eta = 0.1$, $T_l = 0.025$, (c) $\delta = 0.03193$, $\eta = 0.1$, $T_l = 0.025$, (d) $\delta = 0.036$, $\eta = 0.1$, $T_l = 0.025$, (e) $\delta = 0.062$, $\eta = 0.1$, $T_l = 0.025$, (f) $\delta = 0.066$, $\eta = 0.1$, $T_l = 0.025$, (g1, g2) $\delta = 0.015$, $\eta = 0.26$, $T_l = 0.025$ and (h) $\delta = 0.015$, $\eta = 0.2044$, $T_l = 0.025$. Considering $\theta = 20^0 C$, $\gamma = 1/3, \sigma = 4.55$, $\rho = 60$, and $\alpha = 0.00393$ are the other parameters with starting conditions as $\left(i_q (0) = 0.01, i_d (0) = 0.01, \omega (0) = 0.01\right)$ for black curves and $\left(i_q (0) = 0.01, i_d (0) = 60, \omega (0) = 0.01\right)$ for blue curves.

Table 1

Optimized parameters of System (1) obtained from GAs in order to control the chaos encountered in System (1) to S_2.

Parameters	T_l	δ	η
Values	1.8853	0.2089	0.1303

until a stopping criterion is met, such as a predetermined number of generations or achieving an acceptable fitness level or the convergent of the solution of the HNBDCMLT system to one of the desired steady states.

Parameter optimization outcome is the final output of this process that effectively permit the control of the HNBDCMLT system to the desired trajectory. These parameters are expected to enhance system performance, ensuring stability and responsiveness.

The objective function representing the sum of the total squared errors is defined as fitness $= \sum |X_i - S_i|$ where $X_i = \left(i_q, i_d, \omega\right)^t$ and S_i the steady state. The solution of System (1) gives three steady states: $S_1 = \left(5.527627232 \times 10^{-3}, 7.715824939 \times 10^{-6}, 3.3122775 \times 10^{-5}\right)^t$, $S_2 = (0.7843520472, 59.84424005, 1.810482865)^t$ and $S_3 = (-0.7819815494, 59.84518257, -1.815999760)^t$ for $\eta = 0.1$, $\rho = 60$, $\sigma = 4.55$, $\delta = 0.066$, $T_l = 0.025, \alpha = 0.00393, \gamma = 1/3$ and $\theta = 20$ °C. After adjusting the parameters of the GAs, then fixing the parameters $\rho = 60$, $\sigma = 4.55, \alpha = 0.00393, \gamma = 1/3$, $\theta = 20$ °C and optimizing the parameters T_l, δ, η for a more stable convergence of the objective function, the chaos encountered in System (1) can be controlled to the steady state S_2 thanks to the optimized parameters obtained shown in Table 1.

Using the optimized parameters of Table 1, the time evolutions of i_q, i_d, ω, and the objective function are simulated and plotted in Fig. 11.

After adjusting the parameters of the GAs, then fixing the parameters $\rho = 60$, $\sigma = 4.55, \alpha = 0.00393, \gamma = 1/3$, $\theta = 20$ °C and optimizing the parameters T_l, δ, η for a more stable convergence of the objective function, the chaos encountered in System (1) can be controlled to the steady state S_3 thanks to the optimized parameters obtained shown in Table 2.
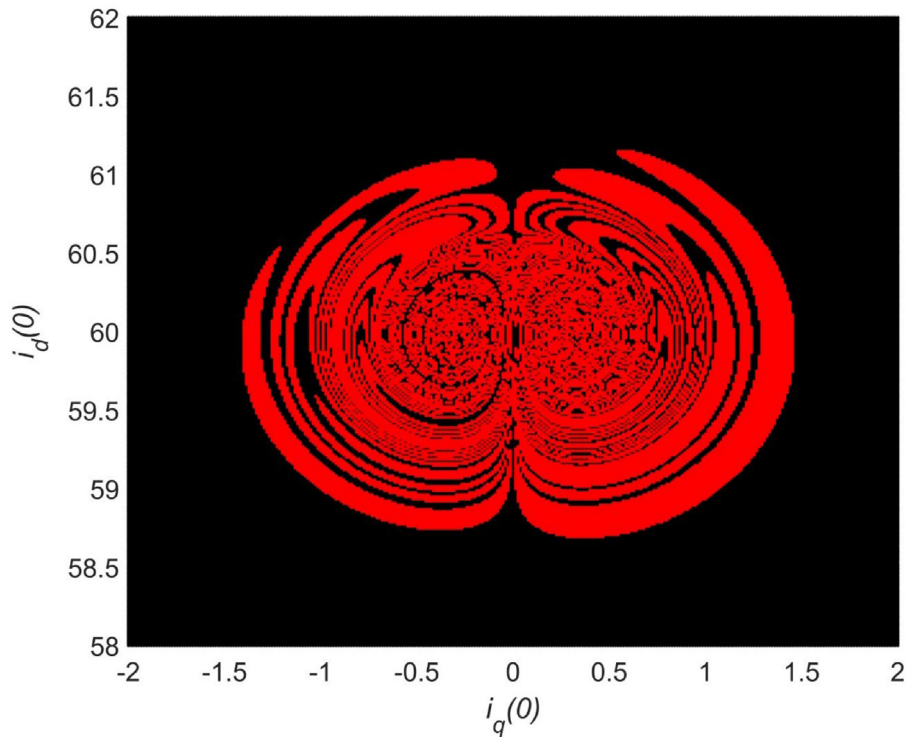
Fig. 8. Basin of attraction giving in the plane $\left(i_q\left(0\right), i_d\left(0\right)\right)$ for $\omega\left(0\right) = 0.01$, $T_l = 0.025$, $\theta = 20\ °C$, $\gamma = 1/3$, $\sigma = 4.55$, $\delta = 0.015$, $\rho = 60$ and $\alpha = 0.00393$.
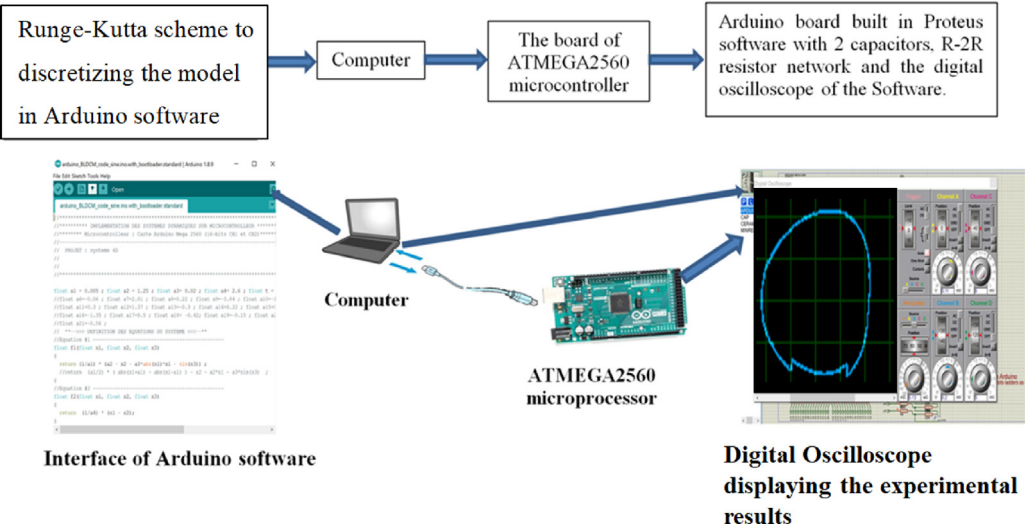

Fig. 9. Diagram of the assembly of microcontroller execution of HNBDCMLT.

Table 2
Optimized parameters of System (1) obtained from GAs in order to control the chaos encountered in System (1) to S_3.

Parameters	T_l	δ	η
Values	3.4715	0.0847	−0.0723

Using the optimized parameters of Table 2, the time evolutions of i_q, i_d, ω, and the objective function are simulated and plotted in Fig. 12.
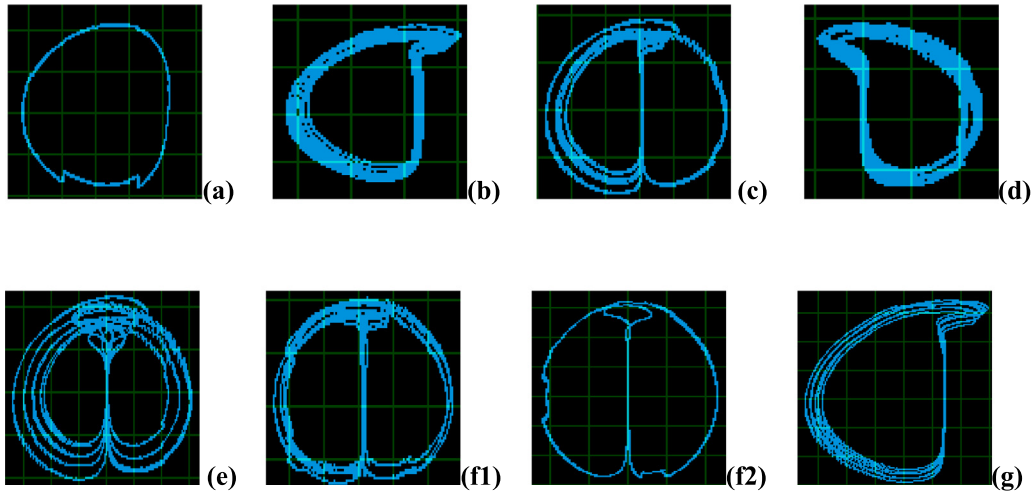
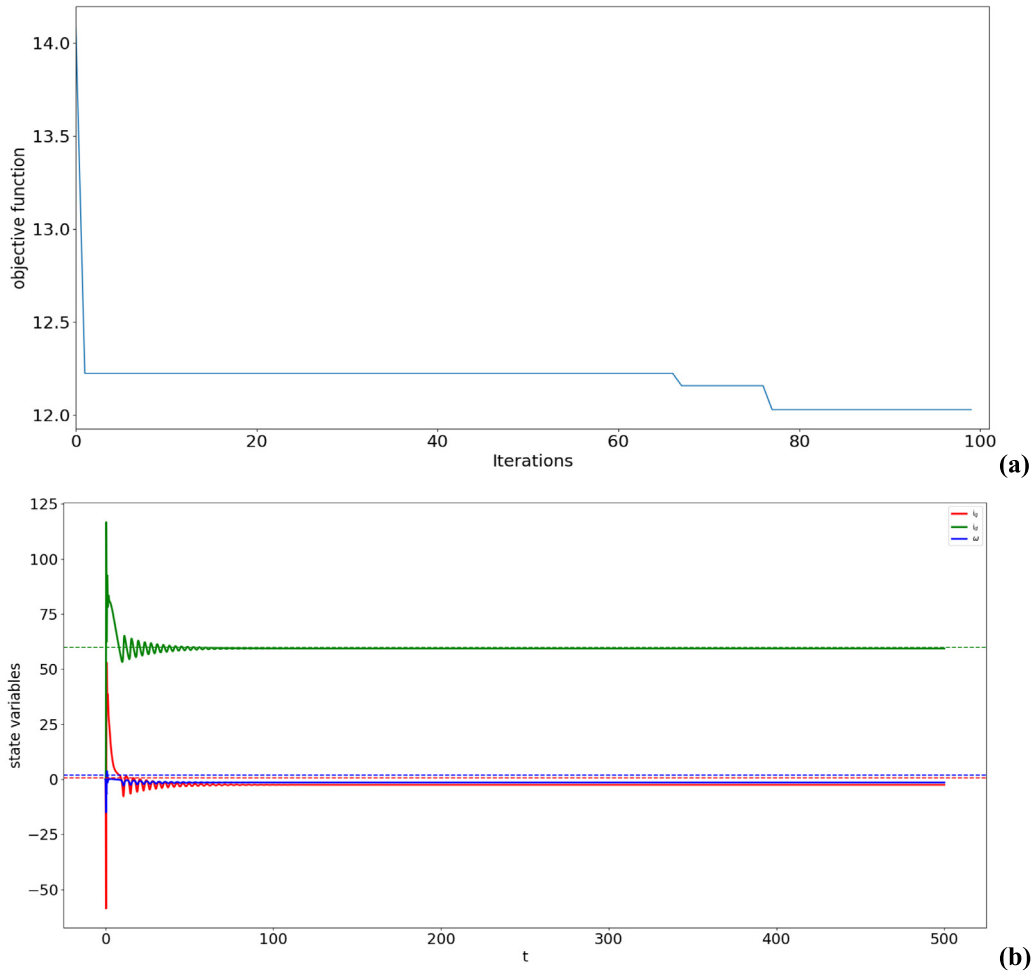**Fig. 10.** Microcontroller results of HNBDCMLT have the same parameters as those in Fig. 7 **(b-h)**.

Fig. 11. (a) Objective function versus the iteration and (b) time evolutions of i_q, i_d, ω for $\rho = 60$, $\sigma = 4.55$, $\alpha = 0.00393$, $\gamma = 1/3$ and $\theta = 20$ °C with the initial states $\left(i_q(0) = 0.01, i_d(0) = 0.01, \omega(0) = 0.01\right)$.
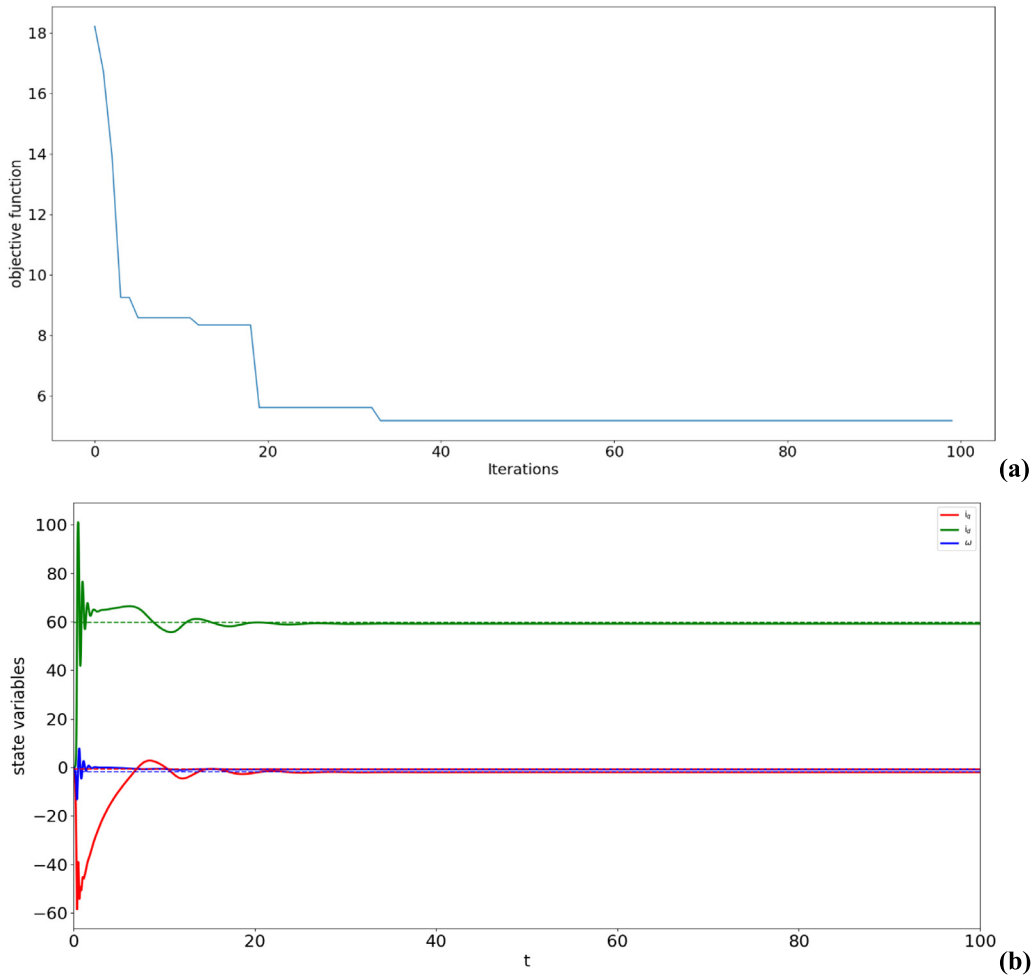
Fig. 12. (a) Objective function versus the iteration and (b) time evolutions of i_q, i_d, ω for $\rho = 60$, $\sigma = 4.55$, $\alpha = 0.00393$, $\gamma = 1/3$ and $\theta = 20$ °C with the initial states $(i_q(0) = 0.01, i_d(0) = 0.01, \omega(0) = 0.01)$.

The objective functions decrease with the number of iterations, then stabilize and no longer vary within the framework of the GAs as depicted in Figs. 11 and 12(a). Figs. 11 and 12(b) reveal that GAs is effective in optimizing system parameters for controlling the chaos encountered in System (1) to the steady state S_i.

The insights gained from HNBDCMLT hold significant promise for industrial applications. Through the optimization of parameters using genetic algorithms, HNBDCMLT can improve efficiency, resulting in lower energy consumption and reduced operational costs. Its capability to manage chaos enhances performance across varying load conditions, making it ideal for precise control in fields such as robotics and manufacturing. Furthermore, improved thermal management contributes to the motor's reliability and longevity, while its adaptability allows for implementation in a wide range of applications, from conveyor systems to electric vehicles. The integration of real-time monitoring capabilities boosts operational efficiency, and the emphasis on energy efficiency aligns with sustainability initiatives by reducing greenhouse gas emissions. To note, HNBDCMLT marks a notable advancement in the realms of industrial automation and energy management.

4. Conclusion

This paper studied the dynamics, microcontroller validation, and annihilation of chaos using genetic algorithms (GAs) for parameters optimization in the heat-affected non-smooth air gap Brushless direct current motor with load torque. The numerical simulations of heat-affected non-smooth air gap Brushless direct current motor with load torque displayed the existence of unstable steady state, stable steady state, Hopf bifurcation, periodic characteristics, antimonotonicity, coexisting attractors, chaotic bubble characteristics, and five different shapes of chaotic characteristics. The dynamical characteristics were attested by the microcontroller execution of heat-affected non-smooth air gap Brushless direct current motor with load torque. By optimizing some parameters of the

heat-affected non-smooth air gap Brushless direct current motor with load torque thanks to the convergence of objective function, it was demonstrated that GAs was able to optimized system parameters leading to annihilation of chaos in the system.

In future research, we will explore 3D representations that illustrate the parametric variations of the system's parameters, along with the error associated with the genetic algorithm's objective function. These representations, aligned with the conclusions from the parameter optimization, will reveal additional parameter combinations that yield acceptable values for the objective function.

CRediT authorship contribution statement

Steve Tchassem Nkengne: Formal analysis. **Buris Peggy Ndemanou:** Formal analysis. **André Chéagé Chamgoué:** Funding acquisition. **Dianorré Tokoue Ngatcha:** Writing – original draft, Validation, Investigation. **Hilaire Bertrand Fotsin:** Validation, Formal analysis. **Sifeu Takougang Kingni:** Supervision, Project administration, Formal analysis.

Declaration of competing interest

The authors have nothing to disclose.

Data availability

No data was used for the research described in the article.

References

[1] Wildi T. Electrical machines, drives, and power systems. 5th ed. Prentice Hall; 2002.
[2] Hemati N. Strange attractors in brushless DC motors. IEEE Trans Circuits Syst I 1994;41:40–5.
[3] Chapman S. Electric machinery fundamentals. Tata McGraw-Hill Education; 2005.
[4] Santoso S, Wayne Beaty H. Electrical engineers. 17th ed. McGraw-Hill Education; 2018.
[5] Venkatesh J, Nkengne ST, Kingni ST, Fotsin HB, Sekhar DC, Rajagopal K. Dynamics, controls of the nonsmooth-air-gap brushless direct current motor under the influence of temperature and embedded in a microcontroller. J Control Autom Electr Syst 2024;35:1121–34.
[6] Lee SH, Yang IJ, Kim WH, Jang IS. Electromagnetic vibration-prediction process in interior permanent magnet synchronous motors using an air gap relative permeance formula. IEEE Access 2021;9:29270–8.
[7] Guoqing L, Qian Z, Lei G, Qiangpeng Y, Gang X, Junqiang Z. Leakage and wear characteristics of finger seal in hot/cold state for aero-engine. Tribol Int 2018;127:209–18.
[8] Konovalov D, Tolstorebrov I, Eikevik TM, Kobalava H, Radchenko M, Hafner A, et al. Recent developments in cooling systems and cooling management for electric motors. Energies 2023;16:7006.
[9] Wang L, Fan J, Wang Z, Zhan B, Li J. Dynamic analysis and control of a permanent magnet synchronous motor with external perturbation. J Dyn Syst Meas Control Trans ASME 2016;138:1–7.
[10] Gnacinski P. Thermal loss of life and load-carrying capacity of marine induction motors. Energy Convers Manag 2014;78:574–83.
[11] Ali SMN, Hanif A, Ahmed Q. Review in thermal effects on the performance of electric motors. In: 2016 int. conf. intell. syst. eng. ICISE 2016, 2016, p. 83–8.
[12] Zocholl SE. Motor analysis and thermal protection. IEEE Trans Power Deliv 1990;5:1275–80.
[13] Nogal Ł, Magdziarz A, Rasolomampionona DD, Łukaszewski P, Sapuła Ł, Szreder R. The laboratory analysis of the thermal processes occurring in low-voltage asynchronous electric motors. Energies 2021;14:2056–68.
[14] Wang Q, Dong E, Du S, Tong T, Yu H, Duan F. Mega-stability and transient chaos analysis of brushless DC motor with winding heat loss. IEEE Int Conf Mechatron Autom 2022;1801–6.
[15] Bottasso CL, Campagnolo F, Croce A, Tibaldi C. Optimization-based study of bend–twist coupled rotor blades for passive and integrated passive/active load alleviation. Wind Energy 2013;16:1149–66.
[16] Saerens E, Furnémont R, Legrand J, Langlois K, López García P, Crispel S, et al. Constant torque mechanisms: A survey. Appl Mech Rev 2022;74:010802.
[17] Khalifa FA, Serry S, Ismail MM, Elhady B. Effect of temperature rise on the performance of induction motors. In: 2009 international conference on computer engineering & systems. IEEE; 2009, p. 549–52.
[18] Hao X, Peng B, Chen Y, Xie G. Transient thermal model of a permanent magnet synchronous planar motor considering spreading thermal resistance. Appl Therm Eng 2015;81:1–9.
[19] Bourne J, Schupbach R, Hollosi B, Di J, Lostetter A, Mantooth HA. Ultra-wide temperature (-230 C to 130 C) DC-motor drive with SiGe asynchronous controller. In: 2008 IEEE aerospace conference. IEEE; 2008, p. 1–15.
[20] Topy AN, Roger J, Pone M, Stephane A, Tsafack K, Kengne R. Chaos and dynamics induced by the amplitude of load torque: Analysis and control. Int Trans Electr Energy Syst 2022;2022:1–23.
[21] Kingni ST, Cheukem A, Nwagoum Tuwa PR, Cheage Chamgoue A, Pham V-T, Jafari S. Synchronous reluctance motor with load vibration perturbation: Analysis, electronic implementation and adaptive backstepping sliding mode control. Iran J Sci Technol Trans Electr Eng 2021;45:645–54.
[22] de la Guerra A, Alvarez-Icaza L. Robust control of the brushless DC motor with variable torque load for automotive applications. Electr Power Compon Syst 2020;48:1–11.
[23] Silwal B, Sergeant P. Thermally induced mechanical stress in the stator windings of electrical machines. Energies 2018;11:2113–30.
[24] Venkataraman B, Godsey B, Premerlani W, Shulman E, Thakur M, Midence R. Fundamentals of a motor thermal model and its applications in motor protection. In: 58th annu. conf. prot. relay eng., vol. 2005. 2005, p. 127–44.
[25] Chakkarapani K, Thangavelu T, Dharmalingam K. Thermal analysis of brushless DC motor using multiobjective optimization. Int Trans Electr Energy Syst 2020;30:1–18.
[26] Srisertpol J, Khajorntraidet C. Estimation of DC motor variable torque using adaptive compensation. In: IEEE, Chinese control and decision conference. 2009.
[27] Park KH, Kim TS, Ahn SC, Hyun DS. Speed control of high-performance brushless DC motor drives by load torque estimation. In: Proc. power electronics specialist conference. 2003.

[28] AL-Samarraie SA, Abbas YK. Design of a nonlinear speed controller for a DC motor system with unknown external torque based on backstepping approach. Iran J Comput Commun Control Syst Eng 2012;12:1–19.

[29] Kamal C, Thyagarajan T, Kalpana D. Optimization techniques for cogging torque reduction and thermal characterization in brushless DC motor. Iran J Sci Technol Trans Electr Eng 2024;48:889–909.

[30] Ngongiah IK, Ramakrishnan B, Natiq H, Pone JRM, Kuiate GF. Josephson junction based on high critical-temperature superconductors: analysis, microcontroller implementation, and suppression of coexisting and chaotic attractors. Eur Phys J B 2022;95:153–66.

[31] Zelinka I. Evolutionary algorithms and deterministic chaos. AIP Conf Proc 2009;1159:26–33.

[32] Javidi M, Hosseinpourfard R. Chaos genetic algorithm instead genetic algorithm. Int Arab J Inf Technol 2015;12:163–8.

[33] Snaselova P, Zboril F. Genetic algorithm using theory of chaos. Procedia Comput Sci 2015;51:316–25.

[34] Premalatha L, VanajaRanjan P. Control of chaos in nonlinear switching circuits by selection of optimal system parameters using genetic algorithm. In: Proc. IEEE int. conf. ind. technol.. 2008.

[35] Richter H, Reinschke KJ. Optimization of local control of chaos by an evolutionary algorithm. Physica D 2000;144:309–34.

[36] Hao JK, Solnon C, Marquis P, Papini O, Prade H. Meta-heuristics and artificial intelligence. In: A guided tour of artificial intelligence research, AI algorithms. Springer; 2020, p. 27–52.

[37] Guessas L, Benmahammed K. Adaptive backstepping and PID optimized by genetic algorithm in control of chaotic. Int J Innov Comput Inf Control 2011;7:5299–312.